# Supplementary Information

## Diversity-driven, efficient exploration of a MOF design space to optimize MOF properties

Tsung-Wei Liu,[†,a] Quan Nguyen[†,b], Adji Bousso Dieng[c]*, Diego A. Gomez-Gualdron[a]*

[a] Department of Chemical and Biological Engineering, Colorado School of Mines, 1601 Illinois St, Golden CO 80401, USA

[b] Department of Computer Science and Engineering, Washington University in St. Louis, 1 Brookings Dr, St. Louis MO 63130, USA

[c] Vertaix, Department of Computer Science, Princeton University, 35 Olden St, Princeton NJ 08540 , USA

† These authors contributed equally

* Corresponding authors: dgomezgualdron@mines.edu

adji@princeton.edu

**Table of Content:**

## S1. Additional molecular simulation details

**Table S1.** Lennard-Jones parameters used in molecular simulations for MOF atoms.

| atom | epsilon(K) | sigma(Å) | atom | epsilon(K) | sigma(Å) | atom | epsilon(K) | sigma(Å) |
|---|---|---|---|---|---|---|---|---|
| O | 48.15 | 3.03 | Sr | 118.26 | 3.24 | Nd | 5.03 | 3.18 |
| N | 37.43 | 3.26 | Pd | 24.15 | 2.58 | Ge | 201.29 | 3.8 |
| C | 47.86 | 3.47 | Ru | 28.18 | 2.64 | Sm | 4.03 | 3.14 |
| F | 36.48 | 3.09 | Pb | 333.63 | 3.83 | Ce | 6.54 | 3.17 |
| B | 47.81 | 3.58 | Hf | 36.23 | 2.8 | Sn | 276.77 | 3.98 |
| P | 161.03 | 3.7 | Ho | 3.52 | 3.04 | Au | 19.63 | 2.93 |
| S | 173.11 | 3.59 | Eu | 4.03 | 3.11 | Ba | 183.17 | 3.3 |
| W | 33.72 | 2.73 | Pr | 5.03 | 3.21 | Pt | 40.26 | 2.45 |
| V | 8.05 | 2.8 | Cs | 22.64 | 4.02 | Mo | 28.18 | 2.72 |
| I | 256.64 | 3.7 | Na | 15.1 | 2.66 | Ra | 203.3 | 3.28 |
| U | 11.07 | 3.02 | He | 10.9 | 2.64 | Ac | 16.61 | 3.1 |
| K | 17.61 | 3.4 | Bi | 260.66 | 3.89 | Th | 13.08 | 3.03 |
| Y | 36.23 | 2.98 | Li | 12.58 | 2.18 | Pa | 11.07 | 3.05 |
| Cl | 142.56 | 3.52 | Se | 216.38 | 3.59 | Np | 9.56 | 3.05 |
| Br | 186.19 | 3.52 | As | 206.32 | 3.7 | Pu | 8.05 | 3.05 |
| H | 22.14 | 2.57 | Rb | 20.13 | 3.67 | Am | 7.05 | 3.01 |
| Zn | 62.4 | 2.46 | Tc | 24.15 | 2.67 | Cm | 6.54 | 2.96 |
| Be | 42.77 | 2.45 | Rh | 26.67 | 2.61 | Bk | 6.54 | 2.97 |
| Cr | 7.55 | 2.69 | La | 8.55 | 3.13 | Cf | 6.54 | 2.95 |
| Fe | 6.54 | 2.59 | Pm | 4.53 | 3.16 | Es | 6.04 | 2.94 |
| Mn | 6.54 | 2.64 | Gd | 4.53 | 3 | Fm | 6.04 | 2.93 |
| Cu | 2.52 | 3.11 | Tb | 3.52 | 3.07 | Md | 5.54 | 2.92 |
| Co | 7.05 | 2.56 | Dy | 3.52 | 3.05 | No | 5.54 | 2.89 |
| Ga | 201.29 | 3.91 | Er | 3.52 | 3.02 | Lw | 5.54 | 2.88 |
| Ti | 8.55 | 2.83 | Tm | 3.02 | 3.01 | | | |
| Sc | 9.56 | 2.94 | Yb | 114.73 | 2.99 | | | |
| Ni | 7.55 | 2.52 | Lu | 20.63 | 3.24 | | | |
| Zr | 34.72 | 2.78 | Ta | 40.76 | 2.82 | | | |
| Mg | 55.86 | 2.69 | Re | 33.21 | 2.63 | | | |
| Ne | 21.14 | 2.89 | Os | 18.62 | 2.78 | | | |
| Ag | 18.12 | 2.8 | Ir | 36.74 | 2.53 | | | |
| In | 276.77 | 4.09 | Hg | 193.74 | 2.41 | | | |
| Cd | 114.73 | 2.54 | Tl | 342.19 | 3.87 | | | |
| Sb | 276.77 | 3.88 | Po | 163.55 | 4.2 | | | |
| Te | 286.84 | 3.77 | At | 142.91 | 4.23 | | | |
| Al | 156 | 3.91 | Rn | 124.8 | 4.25 | | | |
| Si | 156 | 3.8 | Fr | 25.16 | 4.37 | | | |
| Ca | 119.77 | 3.03 | Nb | 29.69 | 2.82 | | | |

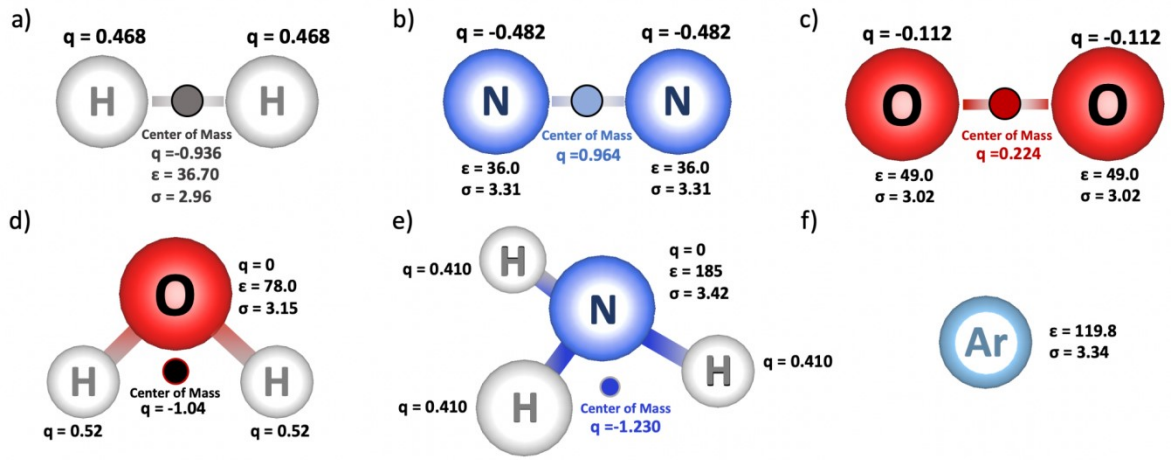


**Figure S1.** Schematic of gas molecule models used in molecular simulations. Partial charge is denoted by q, while LJ parameters are denoted by σ and ε. Hydrogen, nitrogen, oxygen, water, ammonia, and argon molecules are in a), b), c), d), e), and f), respectively.

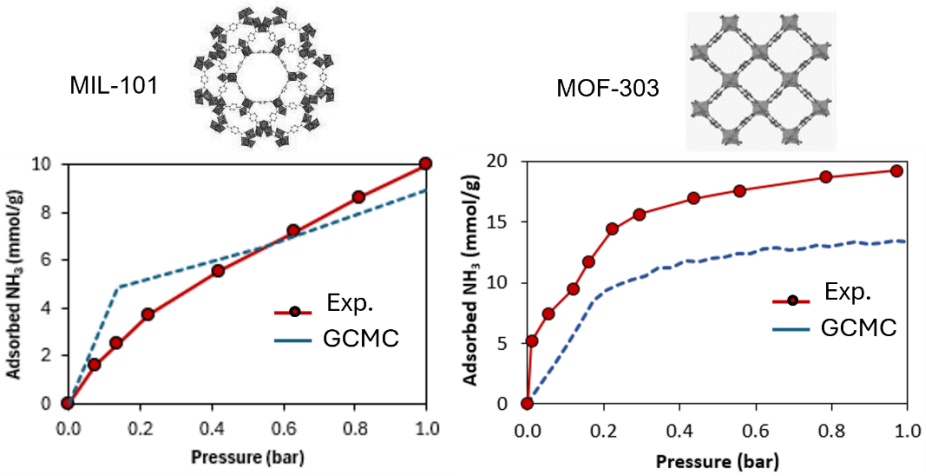


**Figure S2.** Comparison of measured isotherms for two representative MOFs against simulated (GCMC) ones using the force field parameters described in the methods section. MIL-101 is a large-pore MOF with a largest pore diameter (LPD) of 31 Å, and MOF-303 is a small-pore MOF with a LPD of 6 Å. Experimental data taken from refs. 16, 17.

## S2. Surrogate model selection

Molecular simulation data for the 1,000 MOFs randomly sampled from our database was used to guide the selection of the surrogate model. We first use the aforementioned labeled set to train our Gaussian process (GP) model using the kernel function discussed in Section 3.2 in the main text to learn the various relevant metrics. We split the labeled 1,000 MOF dataset into a training and a validation set with a 80%–20% ratio, trained the GP on the training set, and finally observed its performance on the validation set. We compared the GP's performance against two other similarly trained models. Namely, a linear regression and a feedforward neural network (both learn from only the numerical features). The neural network has three hidden layers with 24, 12, and 6 neurons, respectively, and a ReLU activation function after each layer except for the last layer.

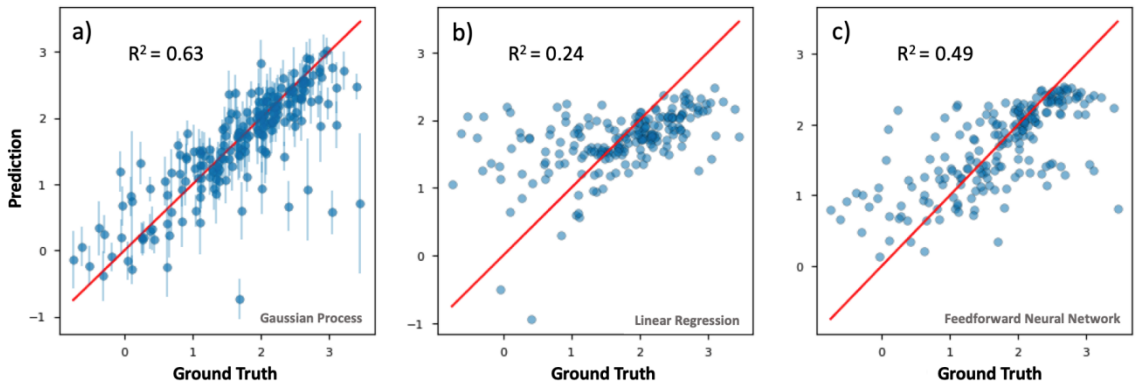


**Figure S3**. Parity plots comparing the prediction of $N_{NH3}^{ads}$—where $N_{NH3}^{ads}$ is the $NH_3$ adsorption loading at 1 bar 300 K—from machine learning with that obtained from molecular simulation (ground truth). Models were trained using molecular simulation data for the randomly 1,000 MOFs. a) Gaussian process, b) linear regression model, and c) feedforward neural network. The red line corresponds to the parity line.

**Fig S3**. shows the parity plots to illustrate the result of learning the property $N_{NH3}^{ads}$ (introduced in Section 2). We see that our GP model performs the best. More crucially, we notice that the GP's predictions that are sufficiently different from the ground truth are often accompanied by high levels of uncertainty (large error bars). This calibrated quantification of uncertainty is a desideratum of the GP and is exactly what enables our VBO approach to search under uncertainty. Finally, we include in **Table S2** relevant performance metrics—mean squared error (MSE), mean absolute error (MAE), and Coefficient of Determination, $R^2$—when we train on different properties and metrics defined in Section 2 of the main text. We see that overall, the GP offers strong predictive performance, consistently achieving lower errors than the other two models. One exception is found in the safety metric, where the GP performs marginally worse than the other two models. We note that this is because the problem of learning the safety metric is a challenging one, as our search space is dominated by data points having labels with zero values (that is, MOFs without sufficient hydrophobicity). While the GP is outperformed by other models, all three models leave room for improvement in terms of predictive accuracy. This relatively poor predictive performance illustrates the difficulty of learning this safety metric. With that said, as we showed in Section 4 of the main text as well as in the next section, the GP still allows us to perform effective optimization of this metric.

**Table S2.** Performance metrics of different machine learning model frameworks

| | Loss Functions | Gaussian process | Linear regression | Feedforward neural network |
|---|---|---|---|---|
| $N_{NH3\|400k}$ | Mean Squared Error | 0.7039 | 0.959 | 0.8274 |
| | Mean Absolute Error | 0.6133 | 0.8025 | 0.6959 |
| | Coefficient of Determination | 0.3443 | 0.1068 | 0.2293 |
| $N_{NH3\|300k}$ | Mean Squared Error | 0.2771 | 0.5666 | 0.3772 |
| | Mean Absolute Error | 0.3376 | 0.5643 | 0.4299 |
| | Coefficient of Determination | 0.6282 | 0.2398 | 0.4939 |
| $\alpha_{NH3}$ | Mean Squared Error | 2.1308 | 2.6776 | 2.5066 |
| | Mean Absolute Error | 1.0566 | 1.2896 | 1.2357 |
| | Coefficient of Determination | 0.2878 | 0.1051 | 0.1623 |
| | Mean Squared Error | 9.5577 | 16.0603 | 12.9641 |

| | | | | |
|---|---|---|---|---|
| $\Delta N_{NH3}$ | Mean Absolute Error | 1.8654 | 2.9361 | 2.3445 |
| | Coefficient of Determination | 0.5898 | 0.3107 | 0.4435 |
| | Mean Squared Error | 9.1432 | 11.266 | 11.0344 |
| $M_{ATS}$ | Mean Absolute Error | 2.1701 | 2.6433 | 2.632 |
| | Coefficient of Determination | 0.3721 | 0.2253 | 0.2422 |
| | Mean Squared Error | 0.0003 | 0.0003 | 0.0003 |
| $M_{ATS}$ | Mean Absolute Error | 0.0052 | 0.005 | 0.004 |
| | Coefficient of Determination | -0.0646 | -0.0336 | -0.0119 |

## S3. Additional details about VBO campaigns

### Feature importance analysis

In Section 3, we designed our kernel function as a weighted sum of individual kernel functions, each capturing a specific aspect about a MOF to compute the similarity between two input MOFs. As the weights for these base kernels are optimized to best fit the data observed throughout the search, we may inspect the optimized values of these weights to gain insights into which features are deemed important for the prediction task at hand. **Table S3** shows the values of these optimized weights for the three search objectives at the end of our search campaign.

In **Table S3**, the weights of the 'linker' and 'node' kernels represent the importance of the building blocks. The 'global' section covers texture properties, including the largest and most accessible pores, pore volume, surface area, volume fraction, and metal-to-metal ratio. 'Pore size distribution' (PSD) implies the variation in pore sizes of the MOFs. For $\Delta N_{NH3}$, the metric is solely based on mono ammonia absorption at two different temperatures. In terms of weight distribution, $\Delta N_{NH3}$ prioritizes the 'global' (44%) and 'PSD' (37%) sections, followed by 'linker' (20%) and 'nodes' (2%). This distribution is consistent with our previous discussions: the pore structure substantially affects the metric values, and detailed information about the linker aids the model in depicting the pore structure, extending beyond mere texture properties. In the second row of $M_{ATS}$'s weight distribution, there is a noticeable shift compared to the first row. 5.5% and 27.2% of importance move from the 'PSD' kernel and 'global' kernel to the 'node' kernel, while the importance allocated to the 'linker' kernel remains unchanged. For $M_{ATS}$, the metric combines ammonia loading and its selectivity over nitrogen and hydrogen. Considering ammonia is polar (unlike nitrogen and hydrogen), promoting selective adsorption of ammonia can be achieved by harnessing Coulomb interactions between the framework and the adsorbate. The charges on metals and neighboring atoms in inorganic nodes bolster Coulomb interactions with ammonia, rendering them more effective than the van der Waals forces with nitrogen and hydrogen. In the third row of metric $M_{ATSTH}$, the 'node' kernel holds 97.6% importance. This metric specifically requires the MOF to adsorb ammonia over water, a more complex task than $M_{ATS}$'s selectivity since both ammonia and water are polar molecules. Coulomb interactions could facilitate the adsorption of both. Consequently, meticulously choosing charges on metals within inorganic nodes becomes a top priority.

**Table S3.** Weights of trained kernels in Gaussian process across three different metrics $\Delta N_{NH3}$, $M_{ATS}$, and $M_{ATSTH}$.

| | $K_{node}$ weight ($w_1$) | $K_{linker}$ weight ($w_2$) | $K_{global}$ weight ($w_3$) | $K_{PSD}$ weight ($w_4$) |
|---|---|---|---|---|
| $\Delta N_{NH3}$ | 0.019 | 0.176 | 0.437 | 0.368 |
| $M_{ATS}$ | 0.353 | 0.169 | 0.165 | 0.313 |
| $M_{ATSTH}$ | 0.976 | 0.014 | 0.005 | 0.005 |

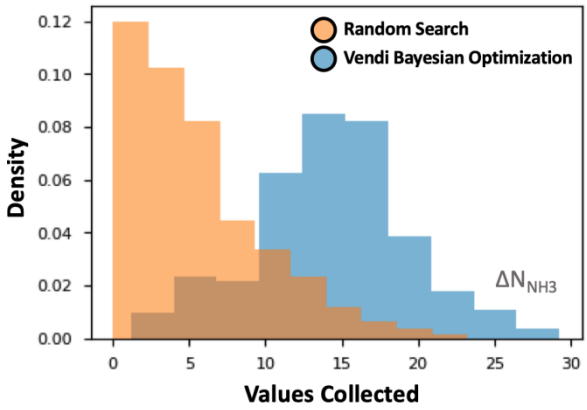


**Figure S4.** Distributions of $\Delta N_{NH3}$ values sampled by VBO (blue) and random search (orange).

## S4. Additional structure-property and elemental composition relationships

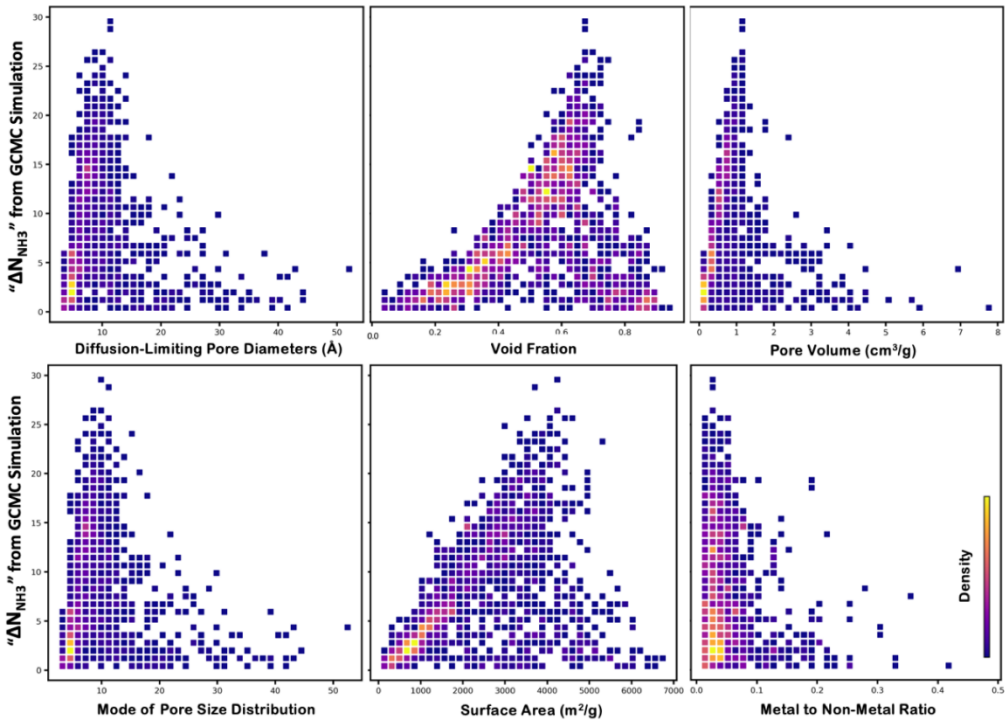


**Figure S5.** Plots of structure-performance relationships. Each square bin corresponds to a combination of $\Delta N_{NH3}$ and MOF property. Where the color followed by the color bar of each bin reflects the number of MOFs normalized by all 1400 MOFs from the randomly 1,000 subset and the 400 MOFs selected by the VBO.

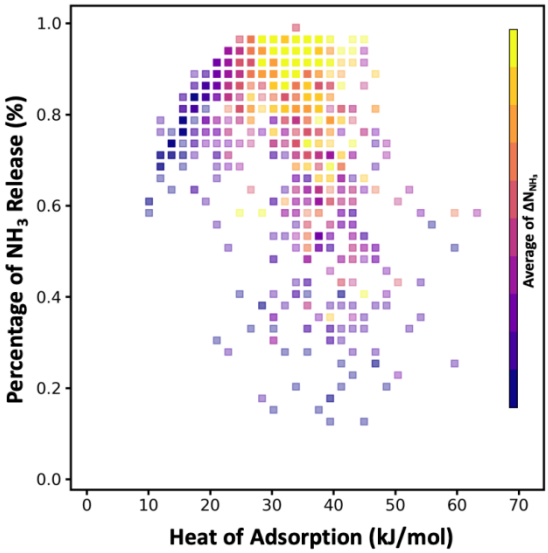


**Figure S6.** Plots of percent of stored $NH_3$ released versus heat of adsorption. Each square bin corresponds to a combination of theoretical energy recovery of $NH_3$ after the desorption from MOF, and the heat of adsorption of $NH_3$ at 300K. Where the color of each bin reflects the average value of $\Delta N_{NH_3}$ in the side color scale, across all MOFs in 1000 random subset and the 400 subset selected by the VBO. The theoretical energy recovery is calculated through values of $\Delta N_{NH3}$ divided by the value of $N_{NH3\text{-}300}$ which is the $NH_3$ loading at 300K 1 bar.

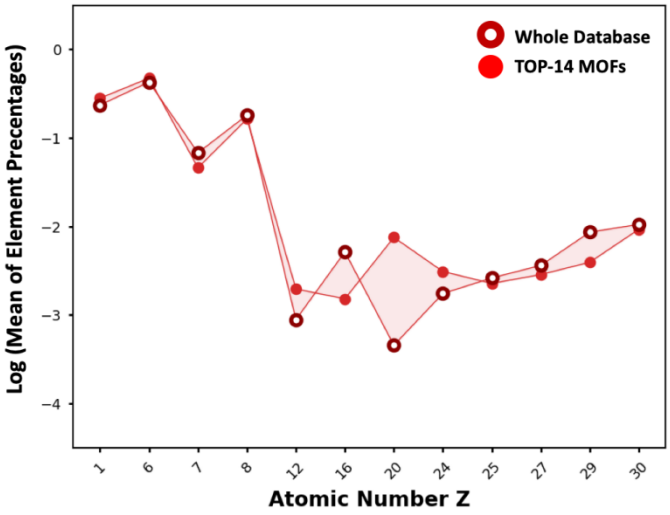


**Figure S7.** The mean of the percentage of elemental content of the top-14 MOFs (solid circles) and the entire database (empty circles) in logarithmic scale. The difference between top-14 MOFs and the entire database is indicated by the shaded area.

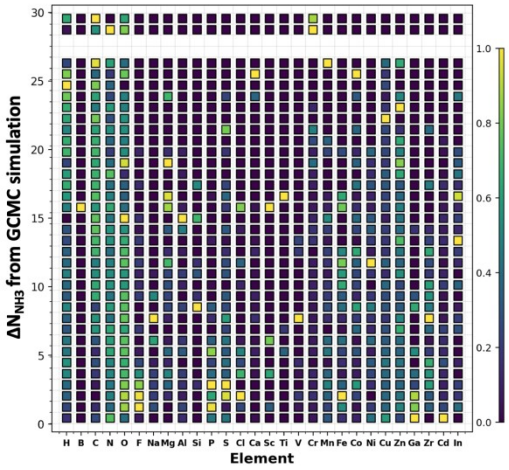


**Figure S8.** The heatmap of the relationship between $\Delta N_{NH3}$ and the common elements content across 1400 MOFs (1000 randoms + 400 selected by VBO). The color in the color bar reflects the element content normalized by values of each bin across the whole column via MinMaxScaler in the sklean package. The value of each bin is the average percentage of element content of all MOFs with corresponding $\Delta N_{NH3}$ and element.

## S5. Additional details about promising MOF designs

**Table S4.** Textural properties and element compositions of the top 20 MOFs of $\Delta N_{NH3}$ value.

| **MOFname** | OPT_lnj_sym_3_on_2_sym_7_mc_4_ntn_edge_1B_2OH | OPT_lnj_sym_3_on_1_sym_7_mc_4_ntn_edge_1B_2OH | WOLREV_clean_CHG | OPT_lvtb_sym_5_mc_2_sym_5_on_9_1B_2OH | JAJZAY_clean_CHG | CEKHIL_clean_CHG | SR_rtw_v1-4c_Cu_1_Ch_v2-5c_bicyclooctane_Ch_1B_2OH_Ch_1x1x2 | PARHEW_clean_CHG | SR_pti_v1-4c_B_Ch_v2-4c_Cu_1_Ch_v3-4c_bicyclooctane_Ch_1B_2NH2_Ch_1x1x2 | PARHAS_clean_CHG | WAQFIG_clean_CHG | WAQDOJ_charged_CHG | OPT_mcn_sym_6_mc_3_sym_3_on_2_ntn_edge_1B_2OH_1B_2OH | SR_pdp_v1-3c_triazine_Ch_v2-6c_bicyclooctane_Ch_v3-4c_Cu_1_Ch_2OH_ch_ntn_edge_1x1x1 | BEFGEA_manual_CHG | HOJLID_clean_CHG | VIDJID_clean_CHG | ENESOH_clean_CHG | DURDAX_clean_CHG | OPT_mcn_sym_6_mc_3_sym_3_on_2_ntn_edge_1B_2OH_ntn_edge |
|---|---|---|---|---|---|---|---|---|---|---|---|---|---|---|---|---|---|---|---|---|
| **Chemical Formula** | $C_{78}O_{25}H_{42}Cr_3$ | $C_{60}N_{18}H_{24}O_{25}Cr_3$ | $C_{29}N_{16}H_{16}Mn_2$ | $C_{17}O_8H_9Cu_1$ | $C_{13}O_4H_3Zn_1$ | $C_{12}N_1H_6O_5Co_1$ | $C_{37}N_3H_{20}O_{11}Cu_1$ | $C_6H_8O_4Ca_1$ | $C_{37}N_8H_{29}O_4Cu_1$ | $C_{24}H_{32}O_{16}Ca_4$ | $C_{22}N_2H_{10}O_{10}S_1Zn_2$ | $C_{57}N_3H_{33}O_{13}Mg_3$ | $C_{48}O_{23}H_{26}Zn_4$ | $C_{112}N_{18}H_{52}O_{36}Cu_3$ | $C_{36}H_{20}O_8In_1$ | $C_{55}N_8H_{43}O_8Zn_2$ | $C_{39}N_9H_{30}O_7Co_3$ | $C_{16}N_{12}H_{16}O_2Cu_1$ | $C_{11}H_5O_4Zn_1$ | $C_{42}H_{22}O_{21}Zn_4$ |
| **$\Delta N_{NH3}$(mmol$_{NH3}$/g$_{-MOF}$)** | 29.2 | 29 | 26.5 | 26.5 | 25.9 | 25.6 | 25.5 | 25.3 | 24.7 | 23.9 | 23.9 | 23.8 | 23.7 | 23.7 | 23.6 | 23.6 | 23.5 | 23 | 23 | 22.9 |
| **Thermal stability (°C)** | 352 | 359 | 316 | 259 | 390 | 340 | 193 | 413 | NA | 416 | 361 | 425 | 309 | NA | 411 | 371 | NA | 587 | 412 | 306 |
| **Release energy penalty (%)** | 9 | 8.5 | 9.1 | 8.6 | 8.2 | 8.7 | 9.8 | 10.5 | 9.2 | 11.4 | 8.8 | 8.1 | 8.5 | 9.6 | 10.1 | 9.8 | 11.3 | 8.4 | 11.5 | 11.6 |
| **Pore Volume(cm$^3$/g)** | 1.2 | 1.12 | 1.11 | 1.1 | 1 | 1.2 | 1.12 | 1.07 | 1.13 | 0.9 | 1.1 | 0.9 | 1.04 | 1 | 1.02 | 1.12 | 1.02 | 1.04 | 1.01 | 0.91 |
| **Void Fraction** | 0.68 | 0.68 | 0.69 | 0.68 | 0.71 | 0.74 | 0.67 | 0.68 | 0.65 | 0.63 | 0.73 | 0.62 | 0.69 | 0.66 | 0.66 | 0.68 | 0.72 | 0.67 | 0.71 | 0.66 |
| **SurfaceArea(m$^2$/g)** | 4310 | 3759 | 4244 | 4211 | 3513 | 4385 | 3986 | 4525 | 4112 | 3953 | 4191 | 3366 | 4017 | 3689 | 3968 | 5225 | 3306 | 4424 | 3844 | 3735 |
| **PoreDi-1 (Å)** | 11.1 | 11.7 | 9.9 | 9.2 | 11.4 | 8.9 | 12 | 7.4 | 12.1 | 6.9 | 8.5 | 10 | 11.3 | 14.6 | 9.3 | 8.3 | 10.7 | 8.4 | 8.5 | 10.9 |
| **PoreDi-2 (Å)** | 11.1 | 11.7 | 9.9 | 9.2 | 11.4 | 8.8 | 11.3 | 7.4 | 10.5 | 6.8 | 8.5 | 10 | 9.8 | 14.4 | 8.8 | 8.2 | 10.7 | 8.4 | 7.6 | 10.8 |
| **APD** | 10.1 | 10.5 | 9.7 | 8.4 | 10.8 | 8.6 | 10.8 | 7.4 | 9.6 | 6.9 | 8.1 | 9.5 | 9.9 | 11.4 | 8.2 | 6.7 | 10.3 | 7.9 | 8.2 | 9.7 |

PoreDi-1 and PoreDi-2 denote the largest pore diameter and the diffusion-limiting pore diameter, respectively, measured in angstroms (Å). APD represents the average pore diameter of the pore size distribution (PSD). The 20 MOFs structures can be found as a supplementary file in cif format.

**Table S5.** Associated publication of top-MOFs belongs to CoRE MOFs database (extant structures), which contains information about relevant synthesis procedure

| CSD refcode | Reference |
|---|---|
| WOLREV | 1 |
| JAJZAY | 2 |
| CEKHIL | 3 |
| PARHEW | 4 |
| PARHAS | 4 |
| WAQFIG | 5 |
| WAQDOJ | 6 |
| BEFGEA | 7 |
| HOJLID | 8 |
| VIDJID | 9 |
| ENESOH | 10 |
| DURDAX | 11 |

**Table S6.** Free energy-based synthesizability criterion of hypothesized MOFs. The Free energy and the Synth. Criteria are calculated through the method by Anderson and Gómez-Gualdrón. [12] Per earlier work by these authors, MOFs have high synthesizability likelihood when the criterion value (last column in Table S5) is below 4.4 kJ/mol per atom

| MOF name | Metal | Metal/Organic Ratio | Free Energy [kJ/mol/atom] | Linear Model | Synth. Criteria [kJ/mol/atom] |
|---|---|---|---|---|---|
| OPT_lnj_sym_3_on_2_sym_7_mc_4_ntn_edge_1B_2OH | Cr | 0.021 | 20.32 | 20.60 | -0.28 |
| OPT_lnj_sym_3_on_1_sym_7_mc_4_ntn_edge_1B_2OH | Cr | 0.024 | 19.03 | 20.69 | -1.66 |
| OPT_lvtb_sym_5_mc_2_sym_5_on_9_1B_2OH | Cu | 0.029 | 12.33 | 16.68 | -4.35 |
| SR_rtw_v1-4c_Cu_1_Ch_v2-5c_bicyclooctane_Ch_1B_2OH_Ch_1x1x2 | Cu | 0.014 | 26.93 | 16.85 | 10.08 |
| SR_pti_v1-4c_B_Ch_v2-4c_Cu_1_Ch_v3-4c_bicyclooctane_Ch_1B_2NH2_Ch_1x1x2 | Cu | 0.013 | 20.22 | 16.86 | 3.36 |
| OPT_mcn_sym_6_mc_3_sym_3_on_2_ntn_edge_1B_2OH_1B_2OH | Zn | 0.041 | 16.38 | 16.88 | -0.50 |
| SR_pdp_v1-3c_triazine_Ch_v2-6c_bicyclooctane_Ch_v3-4c_Cu_1_Ch_1B_2OH_Ch_ntn_edge_1x1x1 | Cu | 0.014 | 18.88 | 16.85 | 2.03 |
| OPT_mcn_sym_6_mc_3_sym_3_on_2_ntn_edge_1B_2OH_ntn_edge | Zn | 0.047 | 12.51 | 16.86 | -4.35 |

**Table S7.** Heat of adsorption of state of art MOFs

| $\Delta N_{NH3}$(mmol$_{NH3}$/g-$_{MOF}$) | Adsorption Temperature (K) | Adsorption Pressure (bar) | Material | Heat of Ads (kJ/mol) | Reference |
|---|---|---|---|---|---|
| 23.5 | 298 | 1 | Ni_acryl_TMA | 45 | 13 |
| 23.9 | 298 | 1 | Mg2(dobpdc) | 146 | 14 |
| 33.9 | 298 | 1 | MIL-53-(OH)2 | 78 | 15 |

## References


(1) Khalilov, A. N.; Khrustalev, V. N.; Aleksandrova, L. V.; Akkurt, M.; Rzayev, R. M.; Bhattarai, A.; Mamedov, İ. G. Crystal Structure and Hirshfeld Surface Analysis of 2,2'-[(3,5-Di-Tert-Butyl-4-Hy-Droxy-Phen-Yl)Methanedi-Yl]Bis-(3-Hy-Droxy-5,5-Di-Methyl-Cyclo-Hex-2-En-1-One). *Acta Crystallogr. E Crystallogr. Commun.* **2023**, *79* (Pt 5), 436–440. DOI: 10.1107/S2056989023003171.

(2) Zhao, D.; Yue, D.; Jiang, K.; Cui, Y.; Zhang, Q.; Yang, Y.; Qian, G. Ratiometric Dual-Emitting MOF⊃dye Thermometers with a Tunable Operating Range and Sensitivity. *J. Mater. Chem. C* **2017**, *5* (7), 1607–1613. DOI: 10.1039/C6TC05203G.

(3) Zou, Y.; Yu, C.; Li, Y.; Lah, M. S. A 3-Dimensional Coordination Polymer with a Rare Lonsdaleite Topology Constructed from a Tetrahedral Ligand. *CrystEngComm* **2012**, *14* (21), 7174. DOI: 10.1039/c2ce26109j.

(4) de Lill, D. T.; Bozzuto, D. J.; Cahill, C. L. Templated Metal-Organic Frameworks: Synthesis, Structures, Thermal Properties and Solid-State Transformation of Two Novel Calcium-Adipate Frameworks. *Dalton Trans.* **2005**, No. 12, 2111–2115. DOI: 10.1039/b502512e.

(5) Jia, Y.-Y.; Liu, X.-T.; Feng, R.; Zhang, S.-Y.; Zhang, P.; He, Y.-B.; Zhang, Y.-H.; Bu, X.-H. Improving the Stability and Gas Adsorption Performance of Acylamide Group Functionalized Zinc Metal–Organic Frameworks through Coordination Group Optimization. *Cryst. Growth Des.* **2017**, *17* (5), 2584–2588. DOI: 10.1021/acs.cgd.7b00119.

(6) Zhai, Q.; Lin, Q.; Wu, T.; Zheng, S.-T.; Bu, X.; Feng, P. Induction of Trimeric [Mg3(OH)(CO2)6] in a Porous Framework by a Desymmetrized Tritopic Ligand. *Dalton Trans.* **2012**, *41* (10), 2866–2868. DOI: 10.1039/c2dt12215d.

(7) Yu, J.; Cui, Y.; Wu, C.; Yang, Y.; Wang, Z.; O'Keeffe, M.; Chen, B.; Qian, G. Second-Order Nonlinear Optical Activity Induced by Ordered Dipolar Chromophores Confined in the Pores of an Anionic Metal-Organic Framework. *Angew. Chem. Int. Ed* **2012**, *51* (42), 10542–10545. DOI: 10.1002/anie.201204160.

(8) Zhu, K.; Vukotic, V. N.; O'Keefe, C. A.; Schurko, R. W.; Loeb, S. J. Metal-Organic Frameworks with Mechanically Interlocked Pillars: Controlling Ring Dynamics in the Solid-State via a Reversible Phase Change. *J. Am. Chem. Soc.* **2014**, *136* (20), 7403–7409. DOI: 10.1021/ja502238a.

(9) Aharen, T.; Habib, F.; Korobkov, I.; Burchell, T. J.; Guillet-Nicolas, R.; Kleitz, F.; Murugesu, M. Novel Co-Based Metal-Organic Frameworks and Their Magnetic Properties Using Asymmetrically Binding 4-(4'-Carboxyphenyl)-1,2,4-Triazole. *Dalton Trans.* **2013**, *42* (21), 7795–7802. DOI: 10.1039/c3dt33000a.

(10) Wang, X.-L.; Rong, X.; Liu, D.-N.; Lin, H.-Y.; Liu, G.-C.; Wang, X.; Song, G. Diverse Polyoxometalate-Based Metal–Organic Complexes Constructed by a Tetrazole- and Pyridyl-Containing Asymmetric Amide Ligand or Its in Situ Transformed Ligand. *CrystEngComm* **2016**, *18* (27), 5101–5109. DOI:

10.1039/C6CE01035K.

(11) Yang, J.; Zhang, L.; Wang, X.; Wang, R.; Dai, F.; Sun, D. Fluorescent Selectivity for Small Molecules of Three Zn-MOFs with Different Topologies Based on a Tetracarboxylate Ligand. *RSC Adv.* **2015**, *5* (77), 62982–62988. DOI: 10.1039/C5RA10391F.

(12) Anderson, R.; Gómez-Gualdrón, D. A. Large-Scale Free Energy Calculations on a Computational Metal–Organic Frameworks Database: Toward Synthetic Likelihood Predictions. *Chem. Mater.* **2020**, *32* (19), 8106–8119. DOI: 10.1021/acs.chemmater.0c00744.

(13) Kim, D. W.; Kang, D. W.; Kang, M.; Choi, D. S.; Yun, H.; Kim, S. Y.; Lee, S. M.; Lee, J.-H.; Hong, C. S. High Gravimetric and Volumetric Ammonia Capacities in Robust Metal-Organic Frameworks Prepared via Double Postsynthetic Modification. *J. Am. Chem. Soc.* **2022**, *144* (22), 9672–9683. DOI: 10.1021/jacs.2c01117.

(14) Kim, D. W.; Kang, D. W.; Kang, M.; Lee, J.-H.; Choe, J. H.; Chae, Y. S.; Choi, D. S.; Yun, H.; Hong, C. S. High Ammonia Uptake of a Metal-Organic Framework Adsorbent in a Wide Pressure Range. *Angew. Chem. Int. Ed* **2020**, *59* (50), 22531–22536. DOI: 10.1002/anie.202012552.

(15) Shi, Y.; Wang, Z.; Li, Z.; Wang, H.; Xiong, D.; Qiu, J.; Tian, X.; Feng, G.; Wang, J. Anchoring LiCl in the Nanopores of Metal-Organic Frameworks for Ultra-High Uptake and Selective Separation of Ammonia. *Angew. Chem. Int. Ed* **2022**, *61* (47), e202212032. DOI: 10.1002/anie.202212032.

(16) Wang, Z.; Li, Z.; Zhang, X.-G., Xia. Q.; Wang, H.; Wang, C.; Wang, Y.; He, H.; Zhao, Yang.; Wang J. Tailoring Multiple Site of Metal-Organic Frameworks for Highly Efficient and Reversible Ammonia Adsorption, *ACS Appl. Mater. Inter.* **2021**, 13 (47), 56025, DOI: 10.1021/acsami.1c14470

(17) Chen, Y.; Zhang, F.; Wang, Y.; Yang, C.; Yang J.; Li, J. Recyclable ammonia uptake of a MIL series of metal-organic frameworks with high structure stability, *Microprous Mesoporous Mater.* **2018**, 258, 170, DOI: 10.1016/j.micromeso.2017.09.013